

4 Stellar Populations of Spectroscopically Decomposed Bulge-Disk for S0 Galaxies from the CALIFA 5 survey

6 MINA PAK,¹ JOON HYEOP LEE,^{1,2} SREE OH,^{3,4} FRANCESCO D'EUGENIO,⁵ MATTHEW COLLESS,^{3,4} HYUNJIN JEONG,¹ AND
7 WOONG-SEOB JEONG^{1,2}

8 ¹*Korea Astronomy and Space Science Institute (KASI), 776 Daeduk-daero, Yuseong-gu, Daejeon 34055, Republic of Korea*

9 ²*Korea University of Science and Technology (UST), 217 Gajeong-ro Yuseong-gu, Daejeon 34113, Republic of Korea*

10 ³*Research School of Astronomy and Astrophysics, Australian National University, Canberra, ACT 2611, Australia*

11 ⁴*ARC Centre of Excellence for All Sky Astrophysics in 3 Dimensions (ASTRO 3D), Australia*

12 ⁵*Sterrenkundig Observatorium, Universiteit Gent, Krijgslaan 281 S9, B-9000 Gent, Belgium*

13 ABSTRACT

14 We investigate the stellar population properties of bulges and disks separately for 34 S0s using
15 integral field spectroscopy from the Calar Alto Legacy Integral Field Area survey. The spatially
16 resolved stellar age and metallicity of bulge and disk components have been simultaneously estimated
17 using the penalized pixel fitting method with photometrically defined weights for the two components.
18 We find a tight correlation between age and metallicity for bulges, while the relation for disks has
19 a larger scatter than that of bulges. This implies that the star formation histories of the disks are
20 more complicated than those of the bulges. Bulges of the high-mass S0s are mostly comparable in
21 metallicity, while bulges appear to be systematically more metal-rich than disks for the low-mass S0s.
22 The ages of bulges and disks in the high-mass S0s appear to increase with local density. The bulge
23 ages of the low-mass S0s also increases with local density, but such a trend is not clear in the disk ages
24 of low-mass S0s. In addition, the age difference between bulge and disk components (ΔAge) tends
25 to increase with local density, both for the high-mass and low-mass S0s. The high-mass S0s have
26 systematically higher ΔAge than the low-mass S0s at given local density. Our results indicate that
27 the stellar mass significantly influences the evolution of S0 galaxies, but the environment also plays an
28 important role in determining the evolution of bulges and disks at given stellar mass.

29 1. INTRODUCTION

30 Galaxies generally contain complex structural compo-
31 nents such as bulges, stellar and gaseous disks, spiral
32 arms, bars, and shells. Decomposing these structures is
33 key to understanding the complex formation and evo-
34 lution history of galaxies (Kormendy 1977; Peng et al.
35 2002; Erwin 2015; Erwin et al. 2015; Johnston et al.
36 2012; Johnston et al. 2014; Tabor et al. 2017; Oh et al.
37 2020; Barsanti et al. 2021). Bulge or spheroidal com-
38 ponents, whose surface brightness profiles roughly fol-
39 low a de Vaucouleurs law (de Vaucouleurs 1948), gen-
40 erally contain an old stellar population with metallic-
41 ities spanning the range from very metal-poor to super
42 metal-rich. They follow the same fundamental plane
43 as elliptical galaxies (Bender et al. 1992; Falc3n-Barroso
44 et al. 2002; Dalla Bont3 et al. 2018). On the other hand,
45 disks generally have exponential surface brightness pro-

46 file (Freeman 1970) have stars with high metallicity and
47 a wide range of ages, together with hydrogen gas, molec-
48 ular clouds, dust and hot gas, heated by star formation
49 and supernovae. The bulge component is dominantly
50 supported by random motion with little net rotation,
51 while the disk component is supported (and flattened)
52 by rotation, making a flattened disk (Cappellari et al.
53 2007; Emsellem et al. 2007; Emsellem et al. 2011; van de
54 Sande et al. 2017). Since the two main components in a
55 galaxy have obviously different properties, the detailed
56 study of kinematics and stellar populations in decom-
57 posed bulges and disks is important for understanding
58 the different processes that contributed to their forma-
59 tion.

60 Since colors can be a proxy for the stellar popula-
61 tions, bulge-disk decomposition has been widely applied
62 to multi-band photometry in the past by fitting analytic
63 functions to the galaxy light distribution in order to re-
64 construct the images of the various components (e.g.
65 Kormendy 1977; Simard 1998; Peng et al. 2002; Erwin
66 2015). The comparison of colors between bulge and disk

67 has shown that disks are bluer than bulges in both spirals and S0s (Bothun & Gregg 1990; Peletier & Balcells
68 1996; Hudson et al. 2010; Head et al. 2014). This implies that disk galaxies have more recent star-formation
69 activity in the outer disk (de Jong 1996) or higher metallicities in their centers (Beckman et al. 1996; Pompei &
70 Natali 1997). However, it has also revealed that some galaxies have negative color gradients within both the
71 bulges and disks of disk galaxies (Terndrup et al. 1994; Peletier & Balcells 1996; Michard & Poulain 2000; Kan-
72 nappan et al. 2009; Head et al. 2014), which implies the presence of older or more metal-rich stellar populations
73 in the outer regions of these galaxies.

74 However, broadband colors cannot resolve the degeneracy between age and metallicity. In order to reliably
75 measure the physical properties of a stellar population, we need to study its spectrum. Decomposition can also
76 be done using spectroscopic data, by taking into account the different kinematic properties of bulges and
77 disks. This involves decomposing the line-of-sight velocity distribution (LOSVD) of a galaxy into kinematic
78 components (Rubin et al. 1992; Kuijken & Merrifield 1993). Indeed, more recently, decomposing has applied
79 the observed spectrum into spectral components (Cocato et al. 2011; Johnston et al. 2012; Tabor et al. 2017;
80 Fraser-McKelvie et al. 2018a; Oh et al. 2018; Méndez-Abreu et al. 2019a; Johnston et al. 2021; Barsanti et al.
81 2021). The spectroscopic decomposition of dynamically distinct bulge and disk components is indispensable to
82 study a detailed exploration of their individual formation histories.

83 A spectroscopic bulge-disk decomposition technique was introduced in Johnston et al. (2012) and Johnston
84 et al. (2014). They decomposed the bulge and disk components using long-slit spectra along the major axes
85 of S0s. They fitted the one-dimensional light profiles as a function of wavelength, and then integrated these
86 profiles to obtain the global bulge and disk spectra for each S0 galaxy. These studies found that the bulge of
87 S0s contains systematically younger and more metal-rich stellar populations. However, they also note that using
88 only their long-slit spectra it is impossible to determine whether these young stellar populations are genuinely
89 associated with the bulge, or if they represent instead contamination by the central disk population.

90 Johnston et al. (2017) applied a new bulge-disk decomposition method to the Mapping Nearby Galaxies at
91 Apache Point Observatory (MaNGA; Bundy et al. 2015) integral field spectroscopy (IFS) data. They obtained
92 image slices at each wavelength and then constructed bulge and disk spectra from the weighted flux at each
93 wavelength, from which they measured the stellar pop-

94 ulations of the two components using the Lick system. Méndez-Abreu et al. (2019b) also carried out a spectro-
95 photometric decomposition for three galaxies from the Calar Alto Legacy Integral Field Area survey (CALIFA;
96 Sánchez et al. 2012). Tabor et al. (2017) introduced simultaneous spectral fitting of the two components using
97 the Python version of the penalized pixel fitting code (pPXF; Cappellari & Emsellem 2004; Cappellari 2017)
98 and applied this to three S0s from the CALIFA survey and to 302 early-type galaxies from the MaNGA survey;
99 the populations and kinematics of the bulge and disk components have been presented in Tabor et al. (2019).
100 Barsanti et al. (2021) also investigated the stellar populations separately in the bulges and the disks of S0s in
101 dense environments using the Sydney-AAO Multi-object Integral field (SAMI) Galaxy Survey. These studies have
102 found interesting constraints on S0 formation, but the consistent and systematic comparison of spectroscopically
103 decomposed bulge and disk components between different environments has rarely been conducted, as yet.

104 Johnston et al. (2014) found that 13 S0s in the Virgo cluster have younger and more metal-rich stellar popu-
105 lations in their bulges than in their disks by analyzing the Lick indices of decomposed bulges and disks from
106 long-slit spectroscopic data. They inferred that a normal spiral galaxy hosting an old bulge and a young star-
107 forming disk may undergo star formation quenching in its disk by gas stripping in the cluster and, simultane-
108 ously, the remaining gas may have fallen into the central bulge, triggering star formation in the bulge for the last
109 time before the galaxy finally fades to a present-day S0. S0s in the clusters could have been through this process
110 in their life.

111 Fraser-McKelvie et al. (2018a) focused on the different formation pathways as a function of stellar mass for S0s
112 by investigating the stellar populations of 279 S0s in the MaNGA survey from Lick indices separately measured
113 in bulges and disks. They found that massive galaxies ($M_{\star} > 10^{10} M_{\odot}$) tend to have older bulges and younger
114 disks, while less massive galaxies ($M_{\star} < 10^{10} M_{\odot}$) tend to have younger bulges and older disks. They argued
115 that the role of environment is negligible. Tabor et al. (2019) performed spectroscopic decomposition of 302
116 early-type galaxies from the MaNGA survey. In their results, bulges and disks have similar ages, but bulges
117 have systematically higher metallicities. The disks appear to have a wide range of both age and metallicity,
118 indicating more complicated star formation histories compared to the bulges. Barsanti et al. (2021) found that
119 bulges are relatively redder and more metal-rich than their surrounding disks, while they did not find any no-

table trend with age. Their results indicate that the redder color in bulges is mainly due to the higher metallicity of the bulge stellar populations. These previous results together indicate possible differences in the bulge and disk formation of S0s between high- and low-density environments, but more consistent and systematic comparisons are necessary to clarify the situation.

Up to now two main formation pathways for S0s have been proposed: the fading of spirals to S0s (e.g. Moran et al. 2007; Laurikainen et al. 2010; Cappellari et al. 2011; Kormendy & Bender 2012; Johnston et al. 2014) and mergers or gravitational interactions (Bekki 1998; Tapia et al. 2017; Diaz et al. 2018; Rizzo et al. 2018). In the scenario of spirals fading to S0s, gas within spiral arms is stripped through environmental mechanisms such as ram pressure stripping (Gunn & Gott 1972), harassment (Moore et al. 1999), thermal evaporation (Cowie & Songaila 1977), and strangulation (Larson et al. 1980), which results in star formation quenching. Secular evolution driven by a bar is also a possible mechanism involved in quenching of spiral galaxies, perhaps inducing a transient starburst by funnelling gas towards the centre and growing the bulge (Combes & Sanders 1981; Kormendy & Kennicutt 2004; Athanasoulas 2013). Bars are common structures in disk galaxies in the local universe: the bar fraction has been reported to be up to $\sim 50\%$ in optical bands (Marinova & Jogee 2007; Reese et al. 2007; Barazza et al. 2008) and rises to $\sim 70\%$ in near-infrared studies (Knapen et al. 2000; Menéndez-Delmestre et al. 2007). Passive spiral galaxies may be evidence for the fading of spirals to S0s. The numerical simulations from Bekki et al. (2002) show how cluster environmental quenching processes can transform spirals into S0s, passing through an intermediate passive spiral phase. The spiral arm structures fade over several Gyrs after the gas is stripped. Recently, however, several observational studies found that passive spirals can be found anywhere from galaxies in isolation to the centers of clusters, and hence no single mechanism can completely explain their origin (Fraser-McKelvie et al. 2016; Fraser-McKelvie et al. 2018b; Pak et al. 2019; Pak et al. 2021; Deeley et al. 2020).

Mergers, accretion or gravitational interactions can also form S0s. The hierarchical models of galaxy formation assume that the bulges of S0s formed by a major merger of disk galaxies or by a sequence of minor merger events (Somerville & Primack 1999). More recent studies in Hopkins et al. (2009) show that disks can survive even 1 : 1 mergers depending on the initial gas content. This scenario seems consistent with the fact that most S0s reside in groups and with observations reporting merging relics in many S0s (Kuntschner et al.

2002; Eliche-Moral et al. 2012; Borlaff et al. 2014). Diaz et al. (2018) introduced a new pathway in lower density environments, where an isolated, high-redshift compact elliptical (cE) galaxy experiences a merger with a smaller gas-rich disk galaxy. The merger remnant effectively transforms into a smooth disk without spiral structure around the cE, which ultimately evolves into an S0.

The goal of this paper is to better understand the evolution of S0s by separately relating bulge and disk stellar populations of CALIFA galaxies to local environment. While previous studies have focused either on clusters (Virgo) or field (MaNGA), this is the first study to use a range of environment consistently. Compared to MaNGA (Husemann et al. 2013), CALIFA (Sánchez et al. 2012) offers better spatial resolution ($2.4''$ in median; García-Benito et al. 2015), hence better accuracy in the photometric decomposition. In addition, bulge-disk decomposition suffers from degeneracies, therefore we use the algorithm of Oh et al. (2020) to overcome this issue. We use a new subroutine of pPXF for dealing with degeneracy in the solutions obtained by both photometrically and kinematically decomposing the bulge and disk components, as recently proposed by Oh et al. (2020). In particular, we focus on the systematic comparison of bulge and disk populations along a wide range of local density, which has been rarely conducted in the previous studies.

This paper is organized as follows. Section 2 describes the galaxy samples adopted from the CALIFA survey. The analysis of data is in Section 3. We present our results in Section 4. Finally, our discussion and conclusions are given in Sections 5 and 6. Throughout the paper we adopt a standard Λ CDM cosmology with $\Omega_m = 0.3$, $\Omega_\Lambda = 0.7$, and $H_0 = 70 \text{ km s}^{-1} \text{ Mpc}^{-1}$.

2. DATA AND SAMPLE SELECTION

The CALIFA survey (Sánchez et al. 2012; Husemann et al. 2013) was carried out using the 3.5-m telescope of the Calar Alto observatory with the PMAS/PPAK spectrograph (Roth et al. 2005; Kelz et al. 2006). The field of view of PPAK is $74'' \times 64''$, which is filled with 382 fibers of $2.7''$ diameter each (Kelz et al. 2006). The galaxies were observed with two spectroscopic setups, using the gratings V500 with a nominal resolution ($\lambda/\Delta\lambda$) of 850 at 5000 \AA (FWHM $\sim 6 \text{ \AA}$) and a wavelength range from 3745 to 7500 \AA , and V1200 with a better spectral resolution of 1650 at 4500 \AA (FWHM $\sim 2.7 \text{ \AA}$) and ranging from 3650 to 4840 \AA . More detailed information about the CALIFA sample, and the observational strategy, is available in the papers of the CALIFA team (Walcher et al. 2014; Sánchez et al. 2012; Husemann et al. 2013;

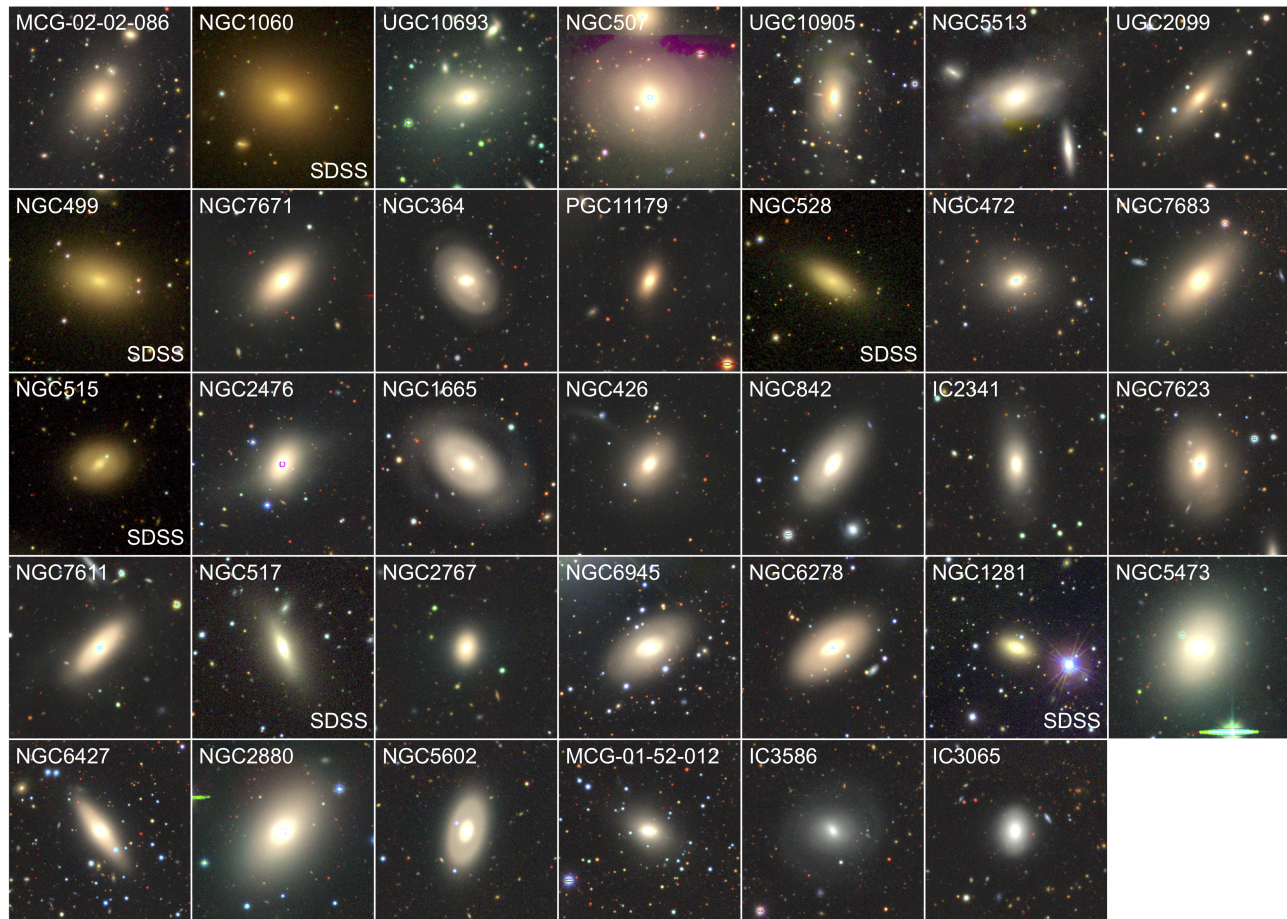


Figure 1. The DECaLS and the SDSS images ($200'' \times 200''$) of the 34 lenticular galaxies. The galaxies are ordered from high to low stellar mass from NASA-Sloan Atlas (NSA, Blanton et al. 2011) catalog. The name of the galaxies is shown in the top corner of each galaxy. **In case the images from SDSS, we label the ‘SDSS’ in the bottom right corner of each image.** North is at the top and east is to the left.

274 García-Benito et al. 2015; and Sánchez et al. 2016). We
 275 here analyzed galaxies using only the V500 data cube.

276 We visually select S0 galaxies from the CALIFA sur-
 277 vey. Using composite color images from the Dark En-
 278 ergy Camera Legacy Survey (DECaLS; Dey et al. 2016)
 279 and the 14 data release of the Sloan Digital Sky Sur-
 280 vey (SDSS DR14; Abolfathi et al. 2018), we selected 87
 281 S0 galaxies showing a prominent spheroidal component
 282 in the center together with a disk-like structure similar
 283 to spirals, but without spiral arms. Then, we reject 25
 284 galaxies with heavily distorted morphology as well as
 285 paired and interacting galaxies, since galaxies with dis-
 286 torted features cannot be successfully constructed in the
 287 structural model from GALFIT (Peng et al. 2002). We
 288 also remove two galaxies closely neighbored by bright
 289 stars, which significantly contaminate galaxy light. Fi-
 290 nally, significantly inclined (edge-on) 26 galaxies are also
 291 removed from the sample, because structural compo-
 292 nents in such galaxies cannot be well decomposed in our
 293 method. This process was performed with visual in-

294 spections of individual galaxies since we found that a
 295 typical disk axis ratio cut does not work for early-type
 296 edge-on galaxies with spherical stellar haloes. The final
 297 sample contains 34 S0 galaxies (see Figure 1). **Our S0s**
 298 **have stellar masses of $9.0 \leq \log(M_*/M_\odot) < 11.5$,**
 299 **based on stellar masses from the NASA-Sloan**
 300 **Atlas (NSA, Blanton et al. 2011) catalog.** For
 301 comparison, we additionally use the nine passive spiral
 302 galaxies as described in Pak et al. (2019).

303 3. ANALYSIS

304 3.1. Photometric decomposition

305 We have performed a photometric bulge-disk decom-
 306 position to obtain the light fraction of both components
 307 at each resolved point in the galaxy. Firstly, the data
 308 cube has been collapsed across the whole wavelength
 309 range to produce a fair single image of the galaxy at
 310 the appropriate spatial resolution. Since the galaxies
 311 in our sample are nearby and therefore S/N of CAL-
 312 IFA data is fairly high, we apply GALFIT (Peng et al.

2002) to this collapsed image directly to fit a Sérsic bulge and an exponential disk, adopting Sérsic index, magnitudes, position angles, flattenings, and scale radii as free parameters, with initial estimates from Méndez-Abreu et al. (2017). The parameters are not available for three passive spirals in Méndez-Abreu et al. (2017). In these cases, we use the resulting values from double Sérsic fits in one-dimension as initial estimates. We also leave the position angles and flattenings of each component as free parameters. GALFIT produces flux models of the bulge and disk components, convolved with the point spread function of the CALIFA data. Finally, we estimate the bulge-to-total (B/T) light ratio for each spaxel as the bulge model flux/(bulge model flux + disk model flux), which is used as a relative flux constraint in the spectral bulge-disk decomposition.

3.2. Spectroscopic decomposition

We spatially bin the CALIFA data by means of the centroidal Voronoi tessellation algorithm of Cappellari & Copin (2003) using the PINGSoft (Rosales-Ortega 2012) software. The minimum signal-to-noise ratio (S/N) per bin for each galaxy is set to be between 5 and 10, which are marginal values for measuring kinematics. The small S/N criterion minimizes the loss of spatial resolution in the binning result, although we may lose many spaxels when we estimate the stellar populations with stricter S/N cuts. However, because our purpose is the bulge-disk decomposition, we decided to secure spatial resolution as fine as possible rather than to bundle up low-S/N spaxels over large spatial areas, which possibly brings a negative effect on the accuracy in the decomposition. In the analysis, we used the age and metallicity averaged over the high-S/N bins for each component, which may guarantee the minimum reliability of the results.

We estimate the luminosity-weighted age and metallicity from the CALIFA data using the single stellar population model templates from Vazdekis et al. (2010), covering a range in ages from 0.06 to 15.8 Gyr and metallicities from -1.71 to 0.22 (a total of 150 templates). The templates are broadened to match the spectral resolution of the CALIFA data using the code LOG_REBIN provided with the pPXF package. As recommended by van de Sande et al. (2017), we first run pPXF for each bin to obtain a precise noise estimate from the residual of the fit and then a second time to clip outliers using the CLEAN keyword in pPXF. In a third iteration, we extract the velocity and velocity dispersion using a 12th-order additive polynomial. Finally, with the extracted velocity and velocity dispersion fixed, the mean age and metallicity are estimated by using a 10th-order multi-

plicative (instead of additive) polynomial. We do not apply the regularization in our analysis.

We fit bulge and disk components, weighted by their relative contributions provided by the photometric decomposition at each spatial coordinate of the data cube. We use the PYTHON version of the pPXF code (Cappellari & Emsellem 2004), updated as described in Cappellari (2017), which allows multiple components with different populations and kinematics to be fitted to spectra simultaneously (Coccatto et al. 2011; Johnston et al. 2014; Tabor et al. 2017). The FRACTION keyword of pPXF allows simultaneous estimation of two components (i.e. a bulge and a disk) with a constraint on the relative weights of the two components:

$$f_{bulge} = \frac{\Sigma w_{bulge}}{\Sigma w_{bulge} + \Sigma w_{disk}}, \quad (1)$$

where w_{bulge} and w_{disk} are the weights assigned to the set of spectral templates for fitting the bulge and disk, respectively. The linear least-squares sub-problem with an exact linear equality constraint (equation 1) can be simplified by adding the following extra constraint requiring only minimal changes to the pPXF algorithm:

$$(f_{bulge} - 1)\Sigma w_{bulge} + f_{bulge}\Sigma w_{disk} \leq \Delta, \quad (2)$$

where Δ regulates the precision required to satisfy inequality (2) and is set to a small number (we use the single precision limit $\Delta = 10^{-9}$). Both the spectral templates and the galaxy spectrum have been normalized to have a mean flux of order unity to satisfy the equality constraint to sufficient numerical accuracy.

The pPXF method can result in unphysical solutions, which is a known issue of simultaneously fitting multiple components. For example, the fit may give a bulge rotation velocity larger than the disk rotation velocity and a bulge velocity dispersion smaller than the disk velocity dispersion. Such cases are obviously unrealistic given our understanding of galaxy structure and we therefore adopt the method introduced in Oh et al. (2020) to deal with them, using a ‘swapping’ subroutine to overcome the degeneracy resulting from two similar local χ^2 minima. This solution is activated when $\sigma_{bulge} + \sigma_{error} < \sigma_{disk}$, where σ_{error} is the error in σ from fitting a single component. Further details of the method are described in Oh et al. (2020). An example of the two-dimensional maps obtained for the kinematics and stellar populations of the bulge and disk components is shown in Figure 2.

The mean age and metallicity of bulge and disk components are summarized in Table 1. The mean values are calculated from bins with bulge S/N, $(S/N)_{bulge} > 30$ and disk S/N, $(S/N)_{disk} > 20$, which are defined by

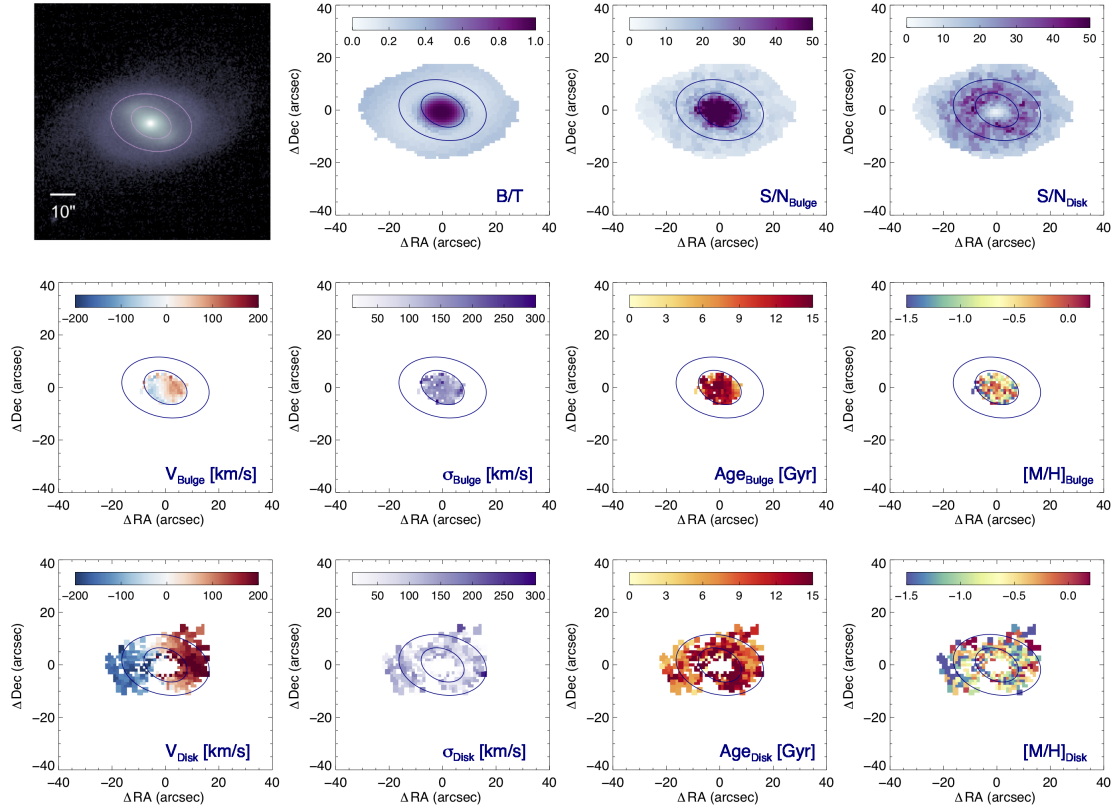


Figure 2. An example of two-dimensional maps of flux, kinematics, and stellar population (UGC 1271). In the first row, the SDSS r-band image, B/T map, bulge S/N, $(S/N)_{bulge} = \sqrt{B/T} \times (S/N)_{continuum}$, and disk S/N, $(S/N)_{disk} = \sqrt{(1 - B/T)} \times (S/N)_{continuum}$ are presented. In the middle and bottom rows, we show V , σ , luminosity-weighted age, and metallicity in the bulge, and the disk components, respectively, whose $(S/N)_{bulge}$ greater than 30 and $(S/N)_{disk}$ greater than 20. The ellipses show the $1R_e$ and $2R_e$ flux contours and their position angles.

$$(S/N)_{bulge} = \sqrt{B/T} \times (S/N)_{continuum}, \text{ and } (S/N)_{disk} = \sqrt{(1 - B/T)} \times (S/N)_{continuum}.$$

4. RESULTS

4.1. The age-metallicity relation of bulge and disk components

Figure 3 presents the luminosity-weighted ages and metallicities of the bulge and disk components. We calculated the mean of total bulge and disk ages and metallicities only when the number of bins with sufficient S/N (> 30 for bulges and > 20 for disks) are 50 or more. The bulges show a tight correlation, with a Spearman correlation coefficient (ρ) of ~ 0.80 . The disks show a larger scatter than bulges, with $\rho \sim 0.66$, and are clearly offset from the robust least-squares linear fit to the bulges. We divide our S0s into a high-mass subsample ($\log M_*/M_\odot > 10.75$; 8 S0s) and a low-mass subsample ($\log M_*/M_\odot \leq 10.75$; 26 S0s, including two dS0); all passive spirals belong to the low-mass subsample. The bulges for low-mass S0s with low metallicity tend to be largely deviated from the fit. The disks of

high-mass S0s are systematically offset from the robust least-squares linear fit to the bulges. The bulges of the passive spirals mostly lie well near the fit to the bulges. The disks of low-mass S0s and passive spirals widely scattered; unlike the disks of high-mass galaxies, the disks of some low-mass galaxies are as old as bulges. Although its faintness makes the signals low, the bulge and disk of two dwarf S0 (dS0) galaxy commonly have young ages.

As seen in Figure 4 and Figure 5, most bulges are older ($\sim 61\%$) and more metal-rich ($\sim 83\%$) than their associated disks. The metallicities of the bulges and disks are comparable for the high-mass S0s with standard deviation of 0.03. The standard deviation of metallicity difference for the low-mass S0s is 0.14. We can more clearly see this in comparing $\Delta \text{Age}_{(Bulge-Disk)}$ and $\Delta [M/H]_{(Bulge-Disk)}$ as a function of stellar mass in Figure 5. Despite the large scatter, the age and metallicity of bulge and disk components appear to be correlated with their global stellar mass. In addition, galaxies with higher stellar masses have pref-

Table 1. The measurements of luminosity-weighted mean age and metallicity for bulge and disk components for all our sample

Name	Stellar mass $\log(M_*/M_\odot)$	Local density $\log\rho_{M,1Mpc}$	Age _{Bulge} (Gyr)	$[M/H]_{Bulge}$	Age _{Disk} (Gyr)	$[M/H]_{Disk}$
Lenticular galaxies						
MCG-02-02-086	11.45	10.43	13.24	-0.15	10.81	-0.15
NGC1060	11.40	10.00	15.53	-0.02	13.69	-0.04
UGC10693	11.17	9.88	11.83	-0.56	9.93	-0.57
NGC0507	11.16	10.47	14.58	-0.32	12.72	-0.35
UGC10905	11.07	8.97	9.04	-0.61	8.98	-0.54
NGC5513	10.89	9.48	11.71	-0.69	9.96	-0.67
UGC02099	10.86	8.65	4.99	-1.12	6.96	-1.10
NGC0499	10.78	10.42	15.39	-0.03	12.59	-0.04
NGC7671	10.68	9.30	14.13	-0.12	14.49	-0.23
NGC0364	10.65	10.56	12.68	-0.40	12.60	-0.46
PGC11179	10.64	—	14.63	-0.13	15.27	-0.21
NGC0528	10.62	10.19	14.62	-0.24	13.66	-0.40
NGC0472	10.61	9.93	8.77	-0.80	7.73	-0.81
NGC7683	10.59	9.90	11.76	-0.31	12.59	-0.31
NGC0515	10.58	10.68	13.53	-0.43	14.39	-0.41
NGC2476	10.58	9.95	12.59	-0.96	12.28	-0.73
NGC0426	10.56	10.32	13.06	-0.24	13.66	-0.25
NGC1665	10.51	8.85	7.30	-0.59	6.64	-0.64
NGC0842	10.50	10.08	11.62	-0.92	12.59	-0.92
IC2341	10.47	9.64	11.15	-1.01	6.62*	-0.85*
NGC7623	10.44	10.80	12.63	-0.38	15.51*	-0.25*
NGC7611	10.43	10.68	12.03	-0.41	8.77	-0.43
NGC0517	10.42	10.38	10.45	-0.62	9.06	-0.84
NGC2767	10.41	10.38	14.40	-0.03	12.82	-0.18
NGC6945	10.40	9.77	10.66*	-0.54*	8.84*	-0.58*
NGC6278	10.39	9.80	12.90	-0.26	15.78	-0.39
NGC1281	10.37	—	15.33	0.00	11.93	-0.08
NGC5473	10.35	9.99	11.21	-0.37	9.43	-0.45
NGC6427	10.31	9.82	8.38	-0.57	11.80	-0.70
NGC2880	10.18	9.55	8.44	-0.27	6.44	-0.53
NGC5602	10.13	9.40	5.90	-0.60	6.45	-0.67
MCG-01-52-012	10.02	9.53	3.22	-1.25	4.05	-1.18
IC3586	9.21	9.76	3.47*	-1.09*	0.95*	-1.33*
IC3065	9.00	9.75	0.75*	-1.20*	2.84	-0.83
Passive spiral galaxies						
UGC02018	10.73	9.02	9.84	-0.97	8.01	-1.05
UGC01271	10.54	10.38	12.59	-0.55	12.39	-0.71
NGC7563	10.52	10.25	14.27	-0.20	14.45*	-0.17*
NGC2553	10.49	10.15	11.53	-0.58	11.66	-0.69
NGC3300	10.40	9.30	12.09	-0.35	12.14	-0.50
NGC0495	10.38	10.51	12.19	-0.41	14.10	-0.46
NGC5794	10.31	10.11	11.57	-0.60	15.85*	-0.57*
NGC5876	10.31	9.78	11.53	-0.31	9.03	-0.40
NGC1666	10.23	9.65	9.69	-0.51	8.05	-0.71

NOTE—Column 1: the name of 34 lenticulars and nine passive spirals. Column 2: the stellar mass from NSA catalog. Column 3: Local density described in section 4.2. Column 4 and 5: the age and metallicity of bulge. Column 6 and 7: the age and metallicity of disk. The symbol of ‘*’ denotes the galaxies having insufficient bins (< 50) in the bulge and the disk.

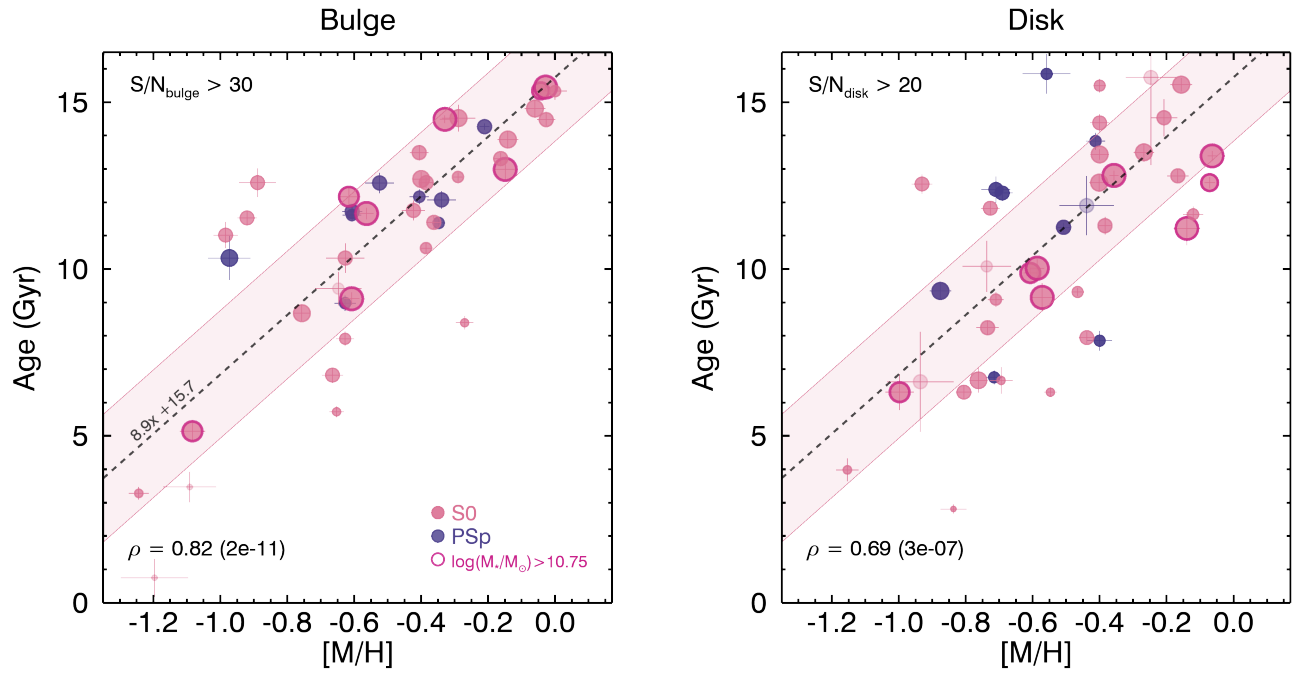


Figure 3. Stellar ages vs. metallicities of the bulge (left panel) and disk (right panel) components for S0s (red circles) and passive spirals (dark blue circles). The size of a symbol is proportional to the stellar mass. The error bar indicates the standard deviation of the mean among the bins in each bulge or disk. The galaxies are divided into a high-mass subsample ($\log M_*/M_\odot > 10.75$; enclosed red open circles) and a low-mass subsample ($\log M_*/M_\odot \leq 10.75$). The fainter symbols indicate galaxies having insufficient bins in the bulge or the disk (< 50). The dashed line in both panels is the linear fit for the bulges with more than 50 bins and the shaded area shows the dispersion about this fit. The Spearman correlation coefficient and the significance of the null hypothesis are indicated in the bottom left of each panel.

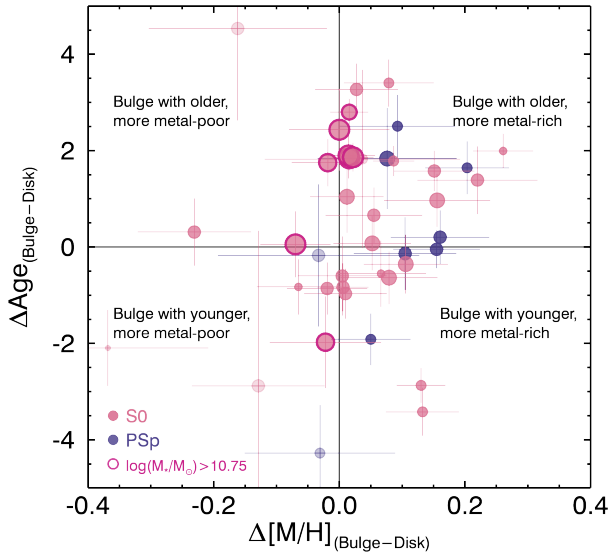


Figure 4. The bulge-disk age difference $\Delta\text{Age}_{(\text{Bulge-Disk})}$ vs. the bulge-disk metallicity difference $\Delta[\text{M}/\text{H}]_{(\text{Bulge-Disk})}$ for individual galaxies. Symbols are the same as Figure 3.

451 essentially a larger $\Delta\text{Age}_{(\text{Bulge-Disk})}$, and the deviation of $\Delta\text{Age}_{(\text{Bulge-Disk})}$ is larger for galaxies with
 452 lower stellar masses. While $\Delta[\text{M}/\text{H}]_{(\text{Bulge-Disk})}$ shows a negative correlations with stellar mass and is almost
 453 zero in the higher-mass galaxies. The passive spirals are also widely dispersed in $\Delta\text{Age}_{(\text{Bulge-Disk})}$, and
 454 $\Delta[\text{M}/\text{H}]_{(\text{Bulge-Disk})}$ is mostly positive. The results of Spearman’s rank coefficient (ρ) and the significance of
 455 deviation (P_0) are summarized in Table 2.

460 4.2. Environment

461 We investigate the environmental effects on the stellar
 462 populations of bulge and disk components. We calculate
 463 projected stellar mass density applying spline kernels
 464 (see Appendix A2 in Lee et al. 2010) by using the galaxies
 465 from the NASA-Sloan Atlas (Blanton et al. 2011)
 466 within the velocity slice of $\pm 500 \text{ km s}^{-1}$ and distance
 467 scale of 1 Mpc for each target galaxy. For completeness,
 468 we use the subsample of galaxies with mass $> 10^{9.5} M_{\odot}$,
 469 but the mass of each target galaxy itself is not consid-
 470 ered in calculating the mass density.

471 Figure 6 presents the age and metallicity of each bulge
 472 and disk as a function of local density. It seems that
 473 both the stellar mass and environment do play a key
 474 role in the stellar populations of each bulge and disk.
 475 The ages of bulges and disks of high-mass S0s appear
 476 to increase with local density ($\rho = 0.79$ for bulges and
 477 $\rho = 0.81$ for disks). For low-mass S0s, the bulge ages also
 478 increase with local density ($\rho = 0.52$), but such a trend
 479 is unclear in the disk ages ($\rho = 0.38$). In addition, the
 480 $\Delta\text{Age}_{(\text{Bulge-Disk})}$ tends to be constant with local den-
 481 sity, both for the high-mass and low-mass S0s. The high-

482 mass S0s have systematically higher $\Delta\text{Age}_{(\text{Bulge-Disk})}$
 483 than the low-mass S0s at given local density.

484 The metallicity of bulges and disks of high-mass S0s
 485 increases with local density ($\rho = 0.74$ for bulges and
 486 $\rho = 0.69$ for disks), but low-mass S0s show no clear
 487 trend ($\rho = 0.16$ for bulges and $\rho = 0.19$ for disks).
 488 For the high-mass S0s, the metallicity in high-density
 489 environments appears to be larger than that in low-
 490 density environments both for bulges and disks, and
 491 $\Delta[\text{M}/\text{H}]_{(\text{Bulge-Disk})}$ is zero on average, regardless of lo-
 492 cal density. The results of Spearman’s rank coefficient
 493 (ρ) and the significance of deviation (P_0) are also sum-
 494 marized in Table 2.

495 5. DISCUSSION

496 Today, it is widely believed that there are two main
 497 pathways for the formation of S0s: (1) fading of spirals
 498 to S0s and (2) merger(s) and/or accretion. From a kine-
 499 matical perspective, it is quite clear that slow-rotating
 500 S0s (stellar $v/\sigma < 0.5$) appear to be found preferen-
 501 tially in low-density environments, in accordance with
 502 the scenario that they are the descendants of mergers/
 503 accretion, while fast-rotating S0s dominate in denser
 504 environments, consistent with the spiral-fading scenario
 505 through the rapid consumption or removal of gas (Dee-
 506 ley et al. 2020; Coccato et al. 2020).

507 However, the detailed analysis of the decomposed
 508 stellar populations implies more complex stories than
 509 those revealed by kinematics only. From our results,
 510 bulges tend to be older in more massive host galaxies
 511 ($\rho = 0.41$), while the ages of the disks depend less on
 512 host galaxy mass ($\rho = 0.37$). This implies that a more
 513 massive galaxy forms its bulge earlier, whereas disk for-
 514 mation is barely dependent on the mass of the host
 515 galaxy and more extended in time. However, even at
 516 a fixed stellar mass, there is a large dispersion in stellar
 517 population properties, suggesting that either stochastici-
 518 ty or another physical factor other than stellar mass
 519 also influences a galaxy star-formation history.

520 Recently, the stellar populations in each component
 521 were analyzed through both line strength measure-
 522 ments and full spectral fitting to obtain estimates of
 523 the luminosity- and mass-weighted properties. John-
 524 ston et al. (2021), where their sample of four S0s in
 525 the Centaurus Cluster and four isolated S0s observed
 526 with MUSE, revealed that the bulges are more metal-
 527 rich than the disks. They interpreted that the majority
 528 of the mass in these galaxies was built up early in the
 529 lifetime of the galaxy, with the bulges and disks forming
 530 from the same material through dissipational processes
 531 at high redshift. The younger stellar populations and
 532 asymmetric features seen in the field S0s may indicate

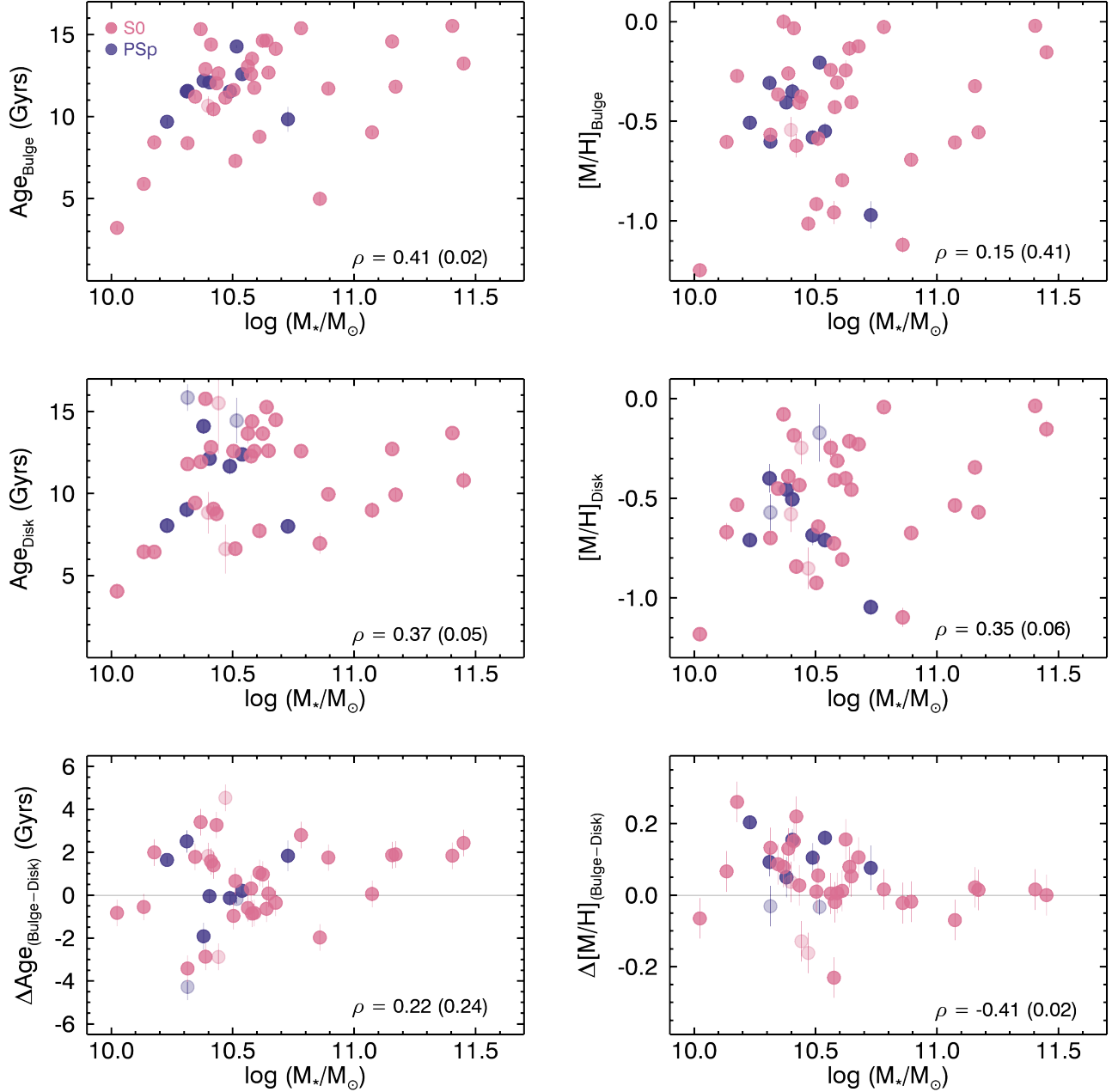


Figure 5. The stellar ages (left panels) and metallicities (right panels) of bulges (top panels), disks (middle panels), and the difference between bulge and disk (bottom panels), all as functions of stellar mass.

533 that these galaxies have been affected more by minor
 534 mergers than the cluster galaxies. Using MaNGA sam-
 535 ple, [Tabor et al. \(2019\)](#) showed bulges of S0s tend to
 536 be consistently more metal-rich than their disk coun-
 537 terparts, and while the ages of both bulge and disk are
 538 comparable, there is an interesting tail of younger and
 539 more metal-poor disks (see figure 2 of [Tabor et al. 2019](#)).
 540 On the other hand, [Méndez-Abreu et al. \(2019a\)](#)
 541 concluded that star formation only ever occurs in the disk
 542 of CALIFA S0s.

543 Since the luminosity-weighted age is sensitive to small
 544 fractions of recently generated stars, our analysis is more
 545 representative of recent star-formation histories than the
 546 mass-weighted age, which is representative of the aver-
 547 age epoch when the bulk of the stars in a galaxy formed.
 548 From the analysis of 279 S0s from the MaNGA sam-
 549 ple, [Fraser-McKelvie et al. \(2018b\)](#) suggested that both
 550 mass and environment are important in the formation
 551 of S0s, but mass plays a more significant role than en-
 552 vironment. However, although there is the caveat of
 553 small number statistics, our results about environments

Table 2. Summary of the Spearman correlation coefficient (ρ) and significance of deviation (P_0) for age and metallicity as a function of stellar mass and density

Y-axis	X-axis	total S0 ρ (P_0)	low-mass S0 ρ (P_0)	high-mass S0 ρ (P_0)
$\text{Age}_{\text{Bulge}}$	$\log(M_*/M_\odot)$	0.41 (0.02)	0.51 (0.01)	0.33 (0.42)
	$\log\rho_{M,1\text{Mpc}}$	0.62 (0.0003)	0.52 (0.02)	0.79 (0.02)
Age_{Disk}	$\log(M_*/M_\odot)$	0.37 (0.05)	0.65 (0.00)	0.36 (0.39)
	$\log\rho_{M,1\text{Mpc}}$	0.45 (0.02)	0.38 (0.10)	0.81 (0.01)
$\Delta\text{Age}_{(\text{Bulge}-\text{Disk})}$	$\log(M_*/M_\odot)$	0.46 (0.01)	0.21 (0.35)	0.05 (0.91)
	$\log\rho_{M,1\text{Mpc}}$	0.39 (0.05)	0.24 (0.33)	0.79 (0.02)
$[\text{M}/\text{H}]_{\text{Bulge}}$	$\log(M_*/M_\odot)$	0.15 (0.41)	0.18 (0.42)	0.43 (0.30)
	$\log\rho_{M,1\text{Mpc}}$	0.39 (0.04)	0.16 (0.47)	0.74 (0.04)
$[\text{M}/\text{H}]_{\text{Disk}}$	$\log(M_*/M_\odot)$	0.35 (0.06)	0.37 (0.09)	0.38 (0.35)
	$\log\rho_{M,1\text{Mpc}}$	0.43 (0.02)	0.19 (0.42)	0.69 (0.06)
$\Delta[\text{M}/\text{H}]_{(\text{Bulge}-\text{Disk})}$	$\log(M_*/M_\odot)$	-0.42 (0.02)	-0.19 (0.40)	0.14 (0.74)
	$\log\rho_{M,1\text{Mpc}}$	0.10 (0.64)	-0.10 (0.68)	0.83 (0.01)

NOTE—The Spearman correlation coefficient (ρ) will be between a value of -1 and $+1$. $\rho = -1$ indicates a perfect negative correlation and $\rho = +1$ indicates a perfect positive correlation.

are robust. Bulges and disks tend to be older as the local density increases. The ages of disks increase for high-mass S0s but show a weak trend for low-mass S0s with local density. As a result, bulges are older than disks in high-density environments. This is consistent with the widely-believed scenario that S0s in dense environment were formed by major merger(s) or rapid collapse at an early epoch before falling into a higher-mass halo. Star formation in the early-formed bulges may have been quenched by some internal mechanisms, such as mass quenching (Kauffmann et al. 2003; Wake et al. 2012) or AGN feedback (Fabian 2012 for a review; George et al. 2019). The bulge quenching may not be due to environmental effects, because environmental effects must have also quenched the star formation in the disks, but disks are slightly younger than bulges at high density in our results. Thus, even after the bulge quenching, star formation in disks must have continued for some time. Alternatively, the disks may have re-formed for a time after the bulge was quenched. As time went on, those S0s may have moved to higher-density environments hostile to star formation in general. Eventually, star formation in the disks may have been also quenched by environmental effects, which explains why disks in high-density environments are older than those in low-density environments.

It is noted that high-mass S0s have slightly younger disks than bulges in high-density environments, but $[\text{M}/\text{H}]$ is almost the same between bulge and disk. If

the disks were created from surrounding matter ejected from early violent mergers, this result seems reasonable. The bulge and disk in an S0 may have similar metallicity because their sources are the same, and the later star formation may have made the disk younger without much altering its metallicity. Strangulation is a valid alternative explanation: the star-forming gas is contained by the surrounding medium and this forces higher recycling rates than possible in the field.

In low-density environments, even if high-mass S0s formed in the same way at an early epoch, they may be more easily rejuvenated by interactions with gas-rich neighboring galaxies (Sanders et al. 1999; Sancisi et al. 2008), a process known to be more frequent in low-density environments with relatively low velocity dispersions (Toomre & Toomre 1972; Lavery & Henry 1988; Byrd & Valtonen 1990). Subsequent new star formation may influence both age and metallicity in the host galaxies; whereas age always becomes younger in such interactions and subsequent star formation, the change in metallicity may largely depend on the properties of the interacting neighbors. In low-density environments, both bulges and disks seem to be influenced by gas accretion. Since gas stripping is not strong in low-density environments, they can keep forming stars using accreted gas and consequently contain relatively younger stars. In this scenario, therefore, ΔAge and $\Delta[\text{M}/\text{H}]$ are almost zero on average, regardless of mass.

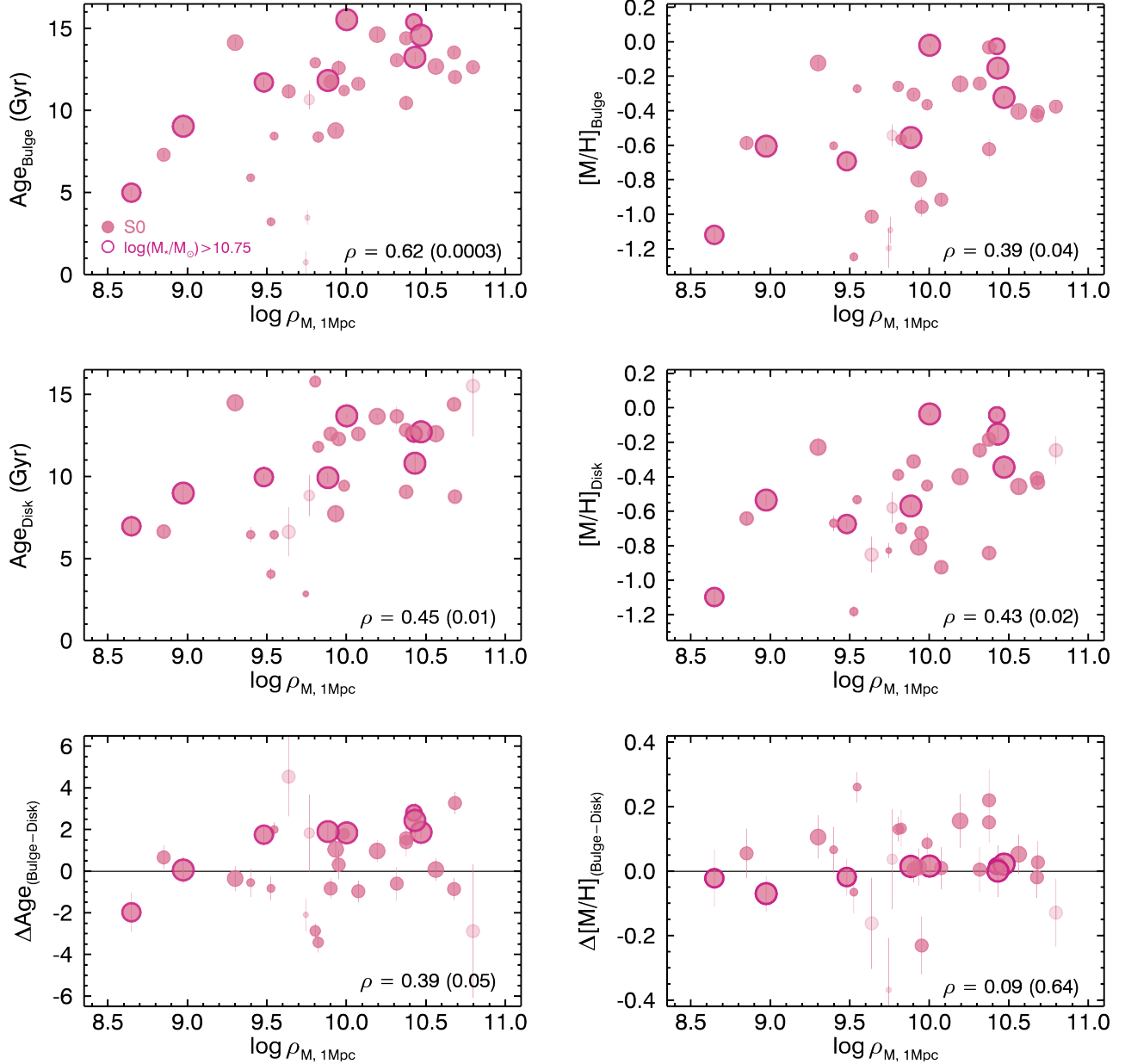


Figure 6. The stellar ages (left panels) and metallicities (right panels) of bulges (top panels), disks (middle panels), and the differences between bulge and disk (bottom panels), as a function of local density; symbols are the same as Figure 3. The Spearman correlation coefficient and significance for all galaxies are shown at the bottom-right of the panels.

611 For low-mass S0s, both ΔAge and $\Delta[\text{M}/\text{H}]$ is almost
 612 constant with local density. At fixed local density, ΔAge
 613 for low-mass S0s is systematically smaller than that
 614 for high-mass S0s; however, low-mass S0s at the high-
 615 est density have larger ΔAge than high-mass S0s at
 616 the lowest density. This result indicates that the impact
 617 on S0 formation of environment is more significant than
 618 that of stellar mass. The bulges and disks of low-mass
 619 S0s are preferentially fast rotators (Figure 7). The
 620 relatively small age difference between bulge and disk
 621 and their fast rotation support the faded-spiral

622 scenario (gas consumption by steady star formation) for
 623 the low-mass S0s, at least in low-density environments.
 624 On the other hand, the S0 galaxies with bulges much
 625 older than disks, found mostly in high-density environ-
 626 ments, may have experienced environmental quenching
 627 (e.g. gas stripping) rather than steady fading. Unlike
 628 the bulges, the ages of the disks do not show a clear
 629 dependence on stellar mass. This may be because disks
 630 are more vulnerable to external influence than bulges.
 631 The large scatter in the age-metallicity relation of disks

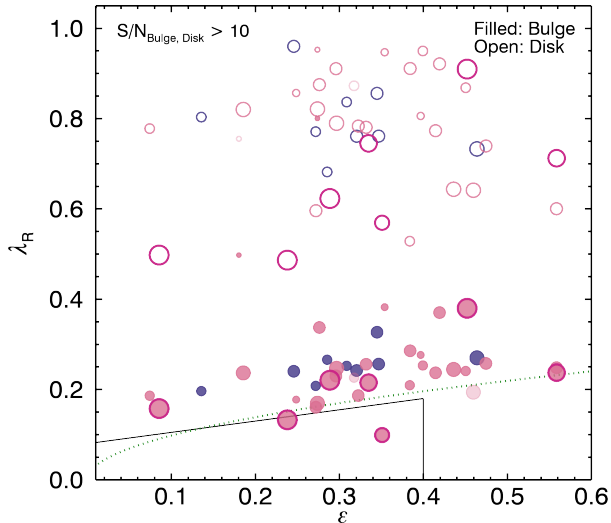


Figure 7. The $\lambda_R - \epsilon$ diagram for bulges and disks; symbols are the same as Figure 3. We have measured λ_R for bulges and disks following the equation (6) from Emsellem et al. (2007). For bulges, λ_R is measured at $R < R_e$.

shows how complex their star formation histories are, compared to those of bulges.

Although it is not majority in our sample, there are 8 out of 34 S0s with younger age and more metal-rich than the corresponding disks, which are similar to the 13 S0s of the Virgo cluster by decomposing long-slit spectroscopic data (Johnston et al. 2014). They are preferentially in lower-density environment in our sample, and most of them are low-mass S0s: **7 low-mass and one high-mass sample**. The 13 S0s from Johnston et al. (2014) are preferentially in lower-density region or outskirts of the cluster with similar projected luminosity density to our sample, even though they are in the Virgo cluster. Their stellar masses ($\log M_*/M_\odot$) taken from NSA catalog also span a range of 9.2 – 10.6 which is the same as our low-mass sample. Johnston et al. (2014) interpreted their results as evidence of late bulge starbursts activated by in-fallen gas, and our sample may share the same formation history with those S0s in the Virgo cluster. Since the Virgo cluster is an irregular and dynamically young cluster, further comparative studies with S0s in more regular and dynamically old clusters would be helpful to fully understand the evolution of S0s in various cluster environments.

6. CONCLUSION

We have analyzed the stellar populations of decomposed bulge and disk components for 34 S0s using data from the CALIFA survey. The decomposed spectra of bulges and disks give several important constraints on the formation histories of S0 galaxies relating to their

stellar mass and environment. In general, the stellar age-metallicity relation of bulges appears to be tight, whereas that of disks shows a negative offset from the bulge relation and has larger scatter. This implies that the star-formation history of the disks may be much more complex than that of the bulges. We found that age has more influence on the offset in the age-metallicity relation between bulge and disk than does metallicity. Most bulges are older than disks, while there is no systematic difference in metallicity.

Our results show that the formation histories of S0 galaxies depend on both their stellar mass and their environment. A more massive S0 galaxy tends to have a larger age difference between its bulge and disk. However, when stellar mass is controlled, an S0 galaxy in a higher-density environment tends to have a larger age difference. From these results, we suggest two scenarios of S0 formation depending on environment.

1. In dense environments, S0s were formed by major merger(s) or rapid collapse at an early epoch. The star formation in the early-formed bulges was quenched by internal mechanisms. After the bulge quenching, the ambient material ejected from the violent merger (re)formed disks, which continued their star formation for a long time (up to 5 Gyr from our results). As the S0s moved to higher-density environments over time, the star formation in disks was eventually also quenched, mainly by environmental effects such as gas-stripping.

2. In low-density environments, bulges were formed at an early epoch in a similar way to the bulges in high-density environments. However, unlike their high-density counterparts, they have been more easily rejuvenated by interactions with gas-rich neighbor galaxies. Both bulges and disks may have been influenced by gas accretion, and so the bulges and disks in low-density environment have very similar stellar populations. The major quenching mechanism in low-density environments may be simple fading through gas consumption by steady star formation.

In short, S0s in low-density environments may be faded spirals, while high-mass S0s in dense environments may have formed via dissipative merger(s), subsequent disk re-building, and finally environmental quenching. These scenarios are consistent with our overall results, but remain somewhat speculative and are too simple to explain all details. Thus, they need to be more rigorously tested and elaborated in further investigations. Most importantly, a much larger sample needs to be an-

713 alyzed in a consistent method to ensure high statistical
714 reliability.

ACKNOWLEDGMENTS

We gratefully thank the anonymous referee for constructive comments that have significantly improved this manuscript. We are also grateful to Yujin Yang for helpful discussions. This study uses data provided by the Calar Alto Legacy Integral Field Area (CALIFA) survey (<http://califa.caha.es/>). Based on observations collected at the Centro Astronómico Hispano Alemán (CAHA) at Calar Alto, operated jointly by the Max-Planck-Institut für Astronomie and the Instituto de Astrofísica de Andalucía (CSIC). Parts of this research were conducted by the Australian Research Council Centre of Excellence for All Sky Astrophysics in 3 Dimensions (ASTRO 3D), through project number CE170100013. FDE acknowledges funding through the H2020 ERC Consolidator Grant 683184.

REFERENCES

- 715 Abolfathi, B., Aguado, D. S., Aguilar, G., et al. 2018,
716 *ApJS*, 235, 42
- 717 Athanassoula, E. 2013, Bars and secular evolution in disk
718 galaxies: Theoretical input, ed. J. Falcón-Barroso & J. H.
719 Knapen, 305
- 720 Barazza, F. D., Jogee, S., & Marinova, I. 2008, *ApJ*, 675,
721 1194
- 722 Barsanti, S., Owers, M. S., McDermid, R. M., et al. 2021,
723 *ApJ*, 906, 100
- 724 Beckman, J. E., Peletier, R. F., Knapen, J. H., Corradi,
725 R. L. M., & Gentet, L. J. 1996, *ApJ*, 467, 175
- 726 Bekki, K. 1998, *ApJL*, 502, L133
- 727 Bekki, K., Couch, W. J., & Shioya, Y. 2002, *ApJ*, 577, 651
- 728 Bender, R., Burstein, D., & Faber, S. M. 1992, *ApJ*, 399,
729 462
- 730 Blanton, M. R., Kazin, E., Muna, D., Weaver, B. A., &
731 Price-Whelan, A. 2011, *AJ*, 142, 31
- 732 Borlaff, A., Eliche-Moral, M. C., Rodríguez-Pérez, C., et al.
733 2014, *A&A*, 570, A103
- 734 Bothun, G. D., & Gregg, M. D. 1990, *ApJ*, 350, 73
- 735 Bundy, K., Bershady, M. A., Law, D. R., et al. 2015, *ApJ*,
736 798, 7
- 737 Byrd, G., & Valtonen, M. 1990, *ApJ*, 350, 89
- 738 Cappellari, M. 2017, *MNRAS*, 466, 798
- 739 Cappellari, M., & Copin, Y. 2003, *MNRAS*, 342, 345
- 740 Cappellari, M., & Emsellem, E. 2004, *PASP*, 116, 138
- 741 Cappellari, M., Emsellem, E., Bacon, R., et al. 2007,
742 *MNRAS*, 379, 418
- 743 Cappellari, M., Emsellem, E., Krajnović, D., et al. 2011,
744 *MNRAS*, 413, 813
- 745 Coccato, L., Morelli, L., Corsini, E. M., et al. 2011,
746 *MNRAS*, 412, L113
- 747 Coccato, L., Jaffé, Y. L., Cortesi, A., et al. 2020, *MNRAS*,
748 492, 2955
- 749 Combes, F., & Sanders, R. H. 1981, *A&A*, 96, 164
- 750 Cowie, L. L., & Songaila, A. 1977, *Nature*, 266, 501
- 751 Dalla Bontà, E., Davies, R. L., Houghton, R. C. W.,
752 D’Eugenio, F., & Méndez-Abreu, J. 2018, *MNRAS*, 474,
753 339
- 754 de Jong, R. S. 1996, *A&AS*, 118, 557
- 755 de Vaucouleurs, G. 1948, *Annales d’Astrophysique*, 11, 247
- 756 Deeley, S., Drinkwater, M. J., Sweet, S. M., et al. 2020,
757 *MNRAS*, 498, 2372
- 758 Dey, A., Rabinowitz, D., Karcher, A., et al. 2016, Society of
759 Photo-Optical Instrumentation Engineers (SPIE)
760 Conference Series, Vol. 9908, Mosaic3: a red-sensitive
761 upgrade for the prime focus camera at the Mayall 4m
762 telescope, 99082C
- 763 Diaz, J., Bekki, K., Forbes, D. A., et al. 2018, *MNRAS*,
764 477, 2030
- 765 Eliche-Moral, M. C., González-García, A. C., Aguerri,
766 J. A. L., et al. 2012, *A&A*, 547, A48

- 767 Emsellem, E., Cappellari, M., Krajnović, D., et al. 2007,
768 MNRAS, 379, 401
- 769 —. 2011, MNRAS, 414, 888
- 770 Erwin, P. 2015, ApJ, 799, 226
- 771 Erwin, P., Saglia, R. P., Fabricius, M., et al. 2015, MNRAS,
772 446, 4039
- 773 Fabian, A. C. 2012, ARA&A, 50, 455
- 774 Falcón-Barroso, J., Peletier, R. F., & Balcells, M. 2002,
775 MNRAS, 335, 741
- 776 Fraser-McKelvie, A., Aragón-Salamanca, A., Merrifield, M.,
777 et al. 2018a, MNRAS, 481, 5580
- 778 Fraser-McKelvie, A., Brown, M. J. I., Pimblet, K., Dolley,
779 T., & Bonne, N. J. 2018b, MNRAS, 474, 1909
- 780 Fraser-McKelvie, A., Brown, M. J. I., Pimblet, K. A.,
781 et al. 2016, MNRAS, 462, L11
- 782 Freeman, K. C. 1970, ApJ, 160, 811
- 783 García-Benito, R., Zibetti, S., Sánchez, S. F., et al. 2015,
784 A&A, 576, A135,
- 785 George, K., Poggianti, B. M., Bellhouse, C., et al. 2019,
786 MNRAS, 487, 3102
- 787 Gunn, J. E., & Gott, III, J. R. 1972, ApJ, 176, 1
- 788 Head, J. T. C. G., Lucey, J. R., Hudson, M. J., & Smith,
789 R. J. 2014, MNRAS, 440, 1690
- 790 Hopkins, P. F., Somerville, R. S., Cox, T. J., et al. 2009,
791 MNRAS, 397, 802
- 792 Hudson, M. J., Stevenson, J. B., Smith, R. J., et al. 2010,
793 MNRAS, 409, 405
- 794 Husemann, B., Jahnke, K., Sánchez, S. F., et al. 2013,
795 A&A, 549, A87
- 796 Johnston, E. J., Aragón-Salamanca, A., & Merrifield, M. R.
797 2014, MNRAS, 441, 333
- 798 Johnston, E. J., Aragón-Salamanca, A., Merrifield, M. R.,
799 & Bedregal, A. G. 2012, MNRAS, 422, 2590
- 800 Johnston, E. J., Häußler, B., Aragón-Salamanca, A., et al.
801 2017, MNRAS, 465, 2317
- 802 Johnston, E. J., Aragón-Salamanca, A., Fraser-McKelvie,
803 A., et al. 2021, MNRAS, 500, 4193
- 804 Kannappan, S. J., Guie, J. M., & Baker, A. J. 2009, AJ,
805 138, 579
- 806 Kauffmann, G., Heckman, T. M., White, S. D. M., et al.
807 2003, MNRAS, 341, 54
- 808 Kelz, A., Verheijen, M. A. W., Roth, M. M., et al. 2006,
809 PASP, 118, 129
- 810 Knapen, J. H., Shlosman, I., & Peletier, R. F. 2000, ApJ,
811 529, 93
- 812 Kormendy, J. 1977, ApJ, 217, 406
- 813 Kormendy, J., & Bender, R. 2012, ApJS, 198, 2
- 814 Kormendy, J., & Kennicutt, Jr., R. C. 2004, ARA&A, 42,
815 603
- 816 Kuijken, K., & Merrifield, M. R. 1993, MNRAS, 264, 712
- 817 Kuntschner, H., Smith, R. J., Colless, M., et al. 2002,
818 MNRAS, 337, 172
- 819 Larson, R. B., Tinsley, B. M., & Caldwell, C. N. 1980, ApJ,
820 237, 692
- 821 Laurikainen, E., Salo, H., Buta, R., Knapen, J. H., &
822 Comerón, S. 2010, MNRAS, 405, 1089
- 823 Lavery, R. J., & Henry, J. P. 1988, ApJ, 330, 596
- 824 Lee, J. H., Lee, M. G., Park, C., & Choi, Y.-Y. 2010,
825 MNRAS, 403, 1930
- 826 Marinova, I., & Jogee, S. 2007, ApJ, 659, 1176
- 827 Méndez-Abreu, J., Sánchez, S. F., & de Lorenzo-Cáceres,
828 A. 2019a, MNRAS, 488, L80
- 829 —. 2019b, MNRAS, 484, 4298
- 830 Méndez-Abreu, J., Ruiz-Lara, T., Sánchez-Menguiano, L.,
831 et al. 2017, A&A, 598, A32
- 832 Menéndez-Delmestre, K., Sheth, K., Schinnerer, E., Jarrett,
833 T. H., & Scoville, N. Z. 2007, ApJ, 657, 790
- 834 Michard, R., & Poulain, P. 2000, A&AS, 141, 1
- 835 Moore, B., Lake, G., Quinn, T., & Stadel, J. 1999,
836 MNRAS, 304, 465
- 837 Moran, S. M., Ellis, R. S., Treu, T., et al. 2007, ApJ, 671,
838 1503
- 839 Oh, S., Kim, K., Lee, J. H., et al. 2018, ApJS, 237, 14
- 840 Oh, S., Colless, M., Barsanti, S., et al. 2020, MNRAS, 495,
841 4638
- 842 Pak, M., Lee, J. H., Jeong, H., et al. 2019, ApJ, 880, 149
- 843 Pak, M., Oh, S., Lee, J. H., et al. 2021, ApJ, 906, 43
- 844 Peletier, R. F., & Balcells, M. 1996, AJ, 111, 2238
- 845 Peng, C. Y., Ho, L. C., Impey, C. D., & Rix, H.-W. 2002,
846 AJ, 124, 266
- 847 Pompei, E., & Natali, G. 1997, A&AS, 124, 129
- 848 Reese, A. S., Williams, T. B., Sellwood, J. A., Barnes, E. I.,
849 & Powell, B. A. 2007, AJ, 133, 2846
- 850 Rizzo, F., Fraternali, F., & Iorio, G. 2018, MNRAS, 476,
851 2137
- 852 Rosales-Ortega, F. F. 2012, ArXiv e-prints.
- 853 Roth, M. M., Kelz, A., Fechner, T., et al. 2005, PASP, 117,
854 620
- 855 Rubin, V. C., Graham, J. A., & Kenney, J. D. P. 1992,
856 ApJL, 394, L9
- 857 Sánchez, S. F., Kennicutt, R. C., Gil de Paz, A., et al.
858 2012, A&A, 538, A8
- 859 Sánchez, S. F., García-Benito, R., Zibetti, S., et al. 2016,
860 A&A, 594, A36
- 861 Sancisi, R., Fraternali, F., Oosterloo, T., & van der Hulst,
862 T. 2008, A&A Rv, 15, 189
- 863 Sanders, D. B., Surace, J. A., & Ishida, C. M. 1999, in
864 Galaxy Interactions at Low and High Redshift, ed. J. E.
865 Barnes & D. B. Sanders, Vol. 186, 289.

- 866 Simard, L. 1998, in *Astronomical Society of the Pacific*
867 *Conference Series*, Vol. 145, *Astronomical Data Analysis*
868 *Software and Systems VII*, ed. R. Albrecht, R. N. Hook,
869 & H. A. Bushouse, 108
- 870 Somerville, R. S., & Primack, J. R. 1999, *MNRAS*, 310,
871 1087
- 872 Tabor, M., Merrifield, M., Aragón-Salamanca, A., et al.
873 2017, *MNRAS*, 466, 2024
- 874 —. 2019, *MNRAS*, 485, 1546
- 875 Tapia, T., Eliche-Moral, M. C., Aceves, H., et al. 2017,
876 *A&A*, 604, A105
- 877 Terndrup, D. M., Davies, R. L., Frogel, J. A., Depoy, D. L.,
878 & Wells, L. A. 1994, *ApJ*, 432, 518
- 879 Toomre, A., & Toomre, J. 1972, *ApJ*, 178, 623
- 880 van de Sande, J., Bland-Hawthorn, J., Fogarty, L. M. R.,
881 et al. 2017, *ApJ*, 835, 104
- 882 Vazdekis, A., Sánchez-Blázquez, P., Falcón-Barroso, J.,
883 et al. 2010, *MNRAS*, 404, 1639
- 884 Wake, D. A., van Dokkum, P. G., & Franx, M. 2012, *ApJL*,
885 751, L44
- 886 Walcher, C. J., Wisotzki, L., Bekeraité, S., et al. 2014,
887 *A&A*, 569, A1